

## Partial-wave representation of the strong-field approximation. II. Coulomb asymmetry in the photoelectron angular distribution of many-electron atoms

Birger Böning <sup>1,2</sup> and Stephan Fritzsche <sup>1,2,3,\*</sup>

<sup>1</sup>*Helmholtz-Institut Jena, 07743 Jena, Germany*

<sup>2</sup>*GSI Helmholtzzentrum für Schwerionenforschung GmbH, 64291 Darmstadt, Germany*

<sup>3</sup>*Theoretisch-Physikalisches Institut, Friedrich-Schiller-Universität Jena, 07743 Jena, Germany*



(Received 7 October 2022; accepted 6 February 2023; published 15 February 2023)

Strong-field ionization experiments are routinely performed with different atomic targets. While these experiments helped reveal many details about the light-matter interaction in intense laser fields, the target atoms are often modeled in a rather crude manner by neglecting most of their electronic structure. Until the present, therefore, many above-threshold ionization measurements had been understood only qualitatively, and this especially applies to the ionization with elliptically polarized laser pulses, for which the photoelectron angular distributions are known to exhibit a quite strong (Coulomb) asymmetry. This asymmetry arises from the Coulomb and short-range forces between the photoion and the outgoing field-dressed electron in the continuum. We demonstrate here how the strong-field approximation (SFA) can be combined with atomic structure theory for modeling such target-resolved observations. Using a partial-wave representation of the SFA, we show that this combination reproduces the Coulomb asymmetry for argon and xenon targets in good agreement with previous experiments and especially if a distorted-wave Volkov continuum is applied for the active electron. We therefore conclude that a better account of the initial and final electron waves in strong-field theories will enhance our understanding of ionization phenomena in intense fields.

DOI: [10.1103/PhysRevA.107.023108](https://doi.org/10.1103/PhysRevA.107.023108)

### I. INTRODUCTION

The interaction of intense laser beams with atomic targets has led to new insights into the quantum dynamics on short timescales [1]. In these experiments, more often than not, the electric field of a laser first ionizes one or several electrons from an atom, which subsequently move in the continuum under the influence of the laser field. If the beam parameters are chosen properly, some of the electrons can be driven back to the photoion, leading either by rescattering to high-energy photoelectrons in processes such as high-order above-threshold ionization (ATI) [2,3] and nonsequential double ionization [4] or by recombination to high-energy photons in high-order harmonic generation [5,6].

In typical ATI experiments, however, most of the photoelectrons are simply pushed away from the photoions and are recorded at some detector. In these measurements, the observed energy spectra typically exhibit distinct peaks that are spaced by the photon energy. Moreover, often the angular distribution of photoelectrons is measured as well at fixed energy. If the (strong) electric field of the laser dominates the electron dynamics in the continuum, e.g., for one of the central assumptions of the strong-field approximation (SFA) [7–9], these angular distributions should reflect also the symmetry of the beam’s vector potential [10]. In practice, however, this symmetry has been found to be broken for most neutral targets, particularly if the ionization process is driven by

elliptically polarized beams [11–13]. A (semi)classical analysis of the electronic motion in the continuum showed that this (Coulomb) asymmetry mainly arises from the long-range electrostatic field of the photoion, which affects the photoelectron even after it has been released from the atom [14]. Quantum mechanically, this static field contributes a phase to the wave function of the outgoing electron, which then becomes visible in a rotation of the angular distribution with regard to the (main) polarization axis [12,15].

Within the SFA, indeed, many ionization and recombination measurements in strong fields can be understood qualitatively; this even applies if hydrogenic target atoms are assumed throughout the derivations [16]. If required, further semiempirical corrections are then added to the motion of the photoelectrons as, for instance, for the electrostatic field of the photoion from above. Nonetheless, such an empirical approach is often not directly comparable to the measured data. Slightly better agreement with experiment has been found if the hydrogenic wave functions were replaced by realistic initial states of the active electron [17,18]. An improvement of the predicted spectra and angular distributions is therefore expected if the SFA is combined explicitly with atomic structure theory. However, since the SFA and the many-body theory of atoms are formulated quite differently, such computations still require major efforts and have been performed until now only for a few selected systems [19,20].

In this work we expand our previous partial-wave representation of the SFA [18] by the proper treatment of the atomic target states for computing ATI photoelectron energy spectra and angular distributions. In particular, we apply here

\*s.fritzsche@gsi.de

realistic one-electron wave functions for both the bound and continuum states as directly obtained from atomic structure theory. All ATI spectra are therefore predicted for given target atoms and for elliptically polarized laser pulses. Moreover, different approximations can be applied and compared quite readily with available measurements in order to better understand the major reasons for the Coulomb asymmetry in the photoelectron angular distributions. This comparison reveals that target-specific distorted continuum states, which are dressed by the laser field, lead indeed to the best agreement with experiments and offer a considerable refinement to those approximations as typically applied within the SFA.

The paper is structured as follows. In Sec. II we first recall the standard formulation of the SFA but by expressing the vector potential of the laser beam in a spherical basis (Sec. II A). We also rewrite both the atomic states and the SFA amplitude in a basis of coupled angular momenta in order to describe the active electron as an integral part of the target atom (Sec. II B). The implementation of this combined treatment is then briefly summarized in Sec. II C. In Sec. III we discuss the theoretical spectra as obtained for the three selected targets: lithium, argon, and xenon. Our results nicely demonstrate how the Coulomb asymmetry can be reproduced if the electronic structure of the target atoms is taken into account, particularly for the distorted continuum states of the outgoing photoelectron. A summary is given in Sec. IV.

Note that atomic units ( $m_e = \hbar = e^2/4\pi\epsilon_0 = 1$ ) are used throughout the paper unless stated otherwise.

## II. THEORETICAL FRAMEWORK

Let us follow Ref. [18] and first recall how a partial-wave representation of the SFA can be formulated for modeling the ATI of atomic targets. By using such a partial-wave expansion of the active-electron wave, we are able to rewrite the initial and final electronic states in a basis of coupled angular momentum for the spatial and spin motion of the electron, rather analogously to the standard treatment of many-electron atoms. To specify the geometry of typical strong-field experiments, Fig. 1 displays an atom that is irradiated by a laser pulse of intensity  $I$ , wavelength  $\lambda$ , and ellipticity  $-1 \leq \epsilon \leq 1$ . In this setup, the laser pulse propagates along the  $z$  axis, while the photoelectrons are recorded in spherical coordinates with asymptotic momentum  $\mathbf{p} = (p, \vartheta_p, \varphi_p)$  at the detector. Moreover, in typical ionization experiments, either the energy distribution of photoelectrons ( $\epsilon_p = p^2/2$ ) is measured along a fixed direction or their angular distribution  $W(\vartheta_p = 90^\circ, \varphi_p)$  is recorded as a function of the azimuthal angle  $\varphi_p$  but at fixed energy of the emitted electrons. Because of the interaction of the target electrons with the strong laser field, the photoelectron can absorb more photons than required for overcoming the ionization potential of the target, which then leads to the well-known and equally spaced ATI peaks in the energy spectrum.

To model this nonlinear ionization process, the electromagnetic fields of the laser beam are described by the vector potential  $\mathbf{A}(\mathbf{r}, t)$ . In the electric dipole approximation [ $\mathbf{A}(\mathbf{r}, t) \approx \mathbf{A}(t)$ ] and velocity gauge, this vector potential can

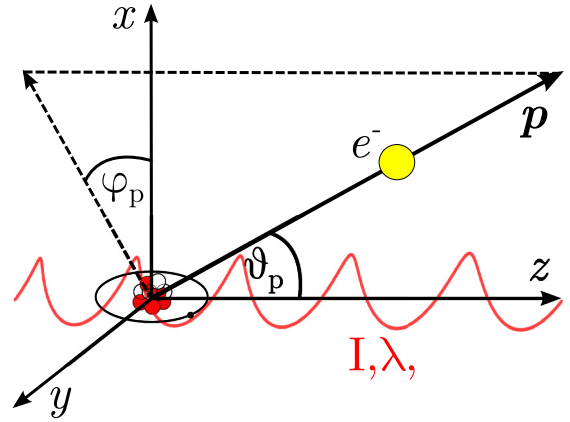


FIG. 1. Geometry of a typical ATI experiment. An atomic target is illuminated by a laser beam, with intensity  $I$ , wavelength  $\lambda$ , and ellipticity  $\epsilon$ , that propagates along the  $z$  axis. After its release, the photoelectron propagates outward and is measured with (asymptotic) momentum  $\mathbf{p} = (p, \vartheta_p, \varphi_p)$  in spherical coordinates.

be written for an elliptically polarized pulse as [21,22]

$$\mathbf{A}(t) = \text{Re}[\mathbf{A}_c(t)] = \frac{1}{2}[\mathbf{A}_c(t) + \mathbf{A}_c^*(t)], \quad (1)$$

with a complex-valued vector potential of the form

$$\mathbf{A}_c(t) = A_0 \mathbf{u} f(t) e^{-i(\omega t + \phi_{\text{CEP}})}. \quad (2)$$

In this expression,  $A_0$  is a (real-valued) amplitude,  $f(t)$  the pulse envelope,  $\omega = 2\pi c/\lambda$  the fundamental frequency, and  $\phi_{\text{CEP}}$  the so-called carrier-envelope phase. Furthermore, the (complex) polarization unit vector

$$\mathbf{u} = \frac{1}{\sqrt{1 + \epsilon^2}} (\mathbf{e}_x + i\epsilon \mathbf{e}_y) \quad (3)$$

defines the orientation of the polarization ellipse and is parametrized in terms of the ellipticity  $-1 \leq \epsilon \leq 1$ .

Within the SFA, the single-active-electron approximation is typically made, which neglects the coupling of the photon field to all except one of the electrons in a target atom. Often, this active electron is initially taken in a hydrogenic  $|1s\rangle$  bound state, though with an effective nuclear charge  $Z_{\text{eff}}$  in order to adjust its binding to the ionization potential of the target. Moreover, due to the interaction with the laser pulse, the electron undergoes a transition from this (undisturbed) initial state into the laser-dressed continuum. In the standard SFA, however, both the correct representation of the initial state of the target atom and the influence of the photoion upon the continuum electron are typically neglected. A more realistic description of the ATI process should therefore account for the (effective) interaction of the active electron in its initial orbital  $|nlm\rangle$  with the other bound electrons as well as the potential of the residual ion that acts upon the outgoing photoelectron. In the following, we will therefore first recall the derivation of the SFA amplitude as well as its transformation into a coupled angular momentum basis for the active electron. This recoupling simplifies the combination with atomic structure theory and, prospectively, will enable us to extend this formalism to many-electron states in modeling strong-field ionization and recombination processes.

### A. Strong-field approximation

The SFA provides an analytical approach to compute the energy- and angle-differential photoionization probability [10,21]

$$\mathbb{P}(\mathbf{p}) = p|T(\mathbf{p})|^2 \quad (4)$$

for the ATI of atoms in strong laser fields in terms of a transition amplitude  $T(\mathbf{p})$ , where  $\mathbf{p}$  is the photoelectron momentum as measured at the detector. In this formalism, a single active electron is initially bound in the state  $|\Psi_i(t)\rangle$  and, due to its interaction with the laser field, finally found in the state  $|\Psi_p(t)\rangle$  with asymptotic momentum  $\mathbf{p}$ . The final state of the photoelectron  $|\Psi_p(t)\rangle$  is thereby expressed via the continuum states  $|\chi_p\rangle$ , which we will analyze below.

By neglecting the laser field for the bound system, the initial state is obtained as an eigenstate of the atomic

$$\begin{aligned} T_0(\mathbf{p}, m, m_s, m'_s) &= -i \int_{-\infty}^{\infty} d\tau \langle \chi_p(\tau) | V_{1e}(\mathbf{r}, \tau) | \Psi_i(\tau) \rangle \\ &= -i \sqrt{\frac{2}{\pi}} \mathcal{F}_1[\omega; f; \mathbf{p}] \langle \chi_{s', m'_s} | \chi_{s, m_s} \rangle \left( \sum_{\ell_p=0}^{\infty} \sum_{q=0, \pm 1} (-1)^q u_q Y_{\ell_p, m-q}(\vartheta_p, \varphi_p) \langle \ell m, 1(-q) | \ell_p m - q \rangle \langle \varepsilon_p \ell_p \| \mathbf{p} \| n \ell \rangle \right) \\ &\quad -i \sqrt{\frac{2}{\pi}} \mathcal{F}_1[-\omega; f; \mathbf{p}] \langle \chi_{s', m'_s} | \chi_{s, m_s} \rangle \left( \sum_{\ell_p=0}^{\infty} \sum_{q=0, \pm 1} u_q^* Y_{\ell_p, m+q}(\vartheta_p, \varphi_p) \langle \ell m, 1q | \ell_p m + q \rangle \langle \varepsilon_p \ell_p \| \mathbf{p} \| n \ell \rangle \right) \\ &\quad -i \frac{1}{\sqrt{2\pi}} \mathcal{F}_2[f; \mathbf{p}] \langle \chi_{s', m'_s} | \chi_{s, m_s} \rangle Y_{\ell m}(\vartheta_p, \varphi_p) \langle \varepsilon_p \ell m \| n \ell m \rangle. \end{aligned} \quad (5)$$

In this form, the radial shape of the initial bound state  $|\Psi_i(t)\rangle$  and final continuum state  $|\Psi_p(t)\rangle$  just enters the (reduced) matrix elements  $\langle \varepsilon_p \ell_p \| \mathbf{p} \| n \ell \rangle$  in terms of the (single-electron) orbital functions  $|n \ell\rangle$  and  $|\varepsilon_p \ell_p\rangle$ , respectively. Moreover, the detailed shape of the driving laser pulse is contained in the so-called pulse-shape integrals

$$\mathcal{F}_1[\pm\omega; f; \mathbf{p}] = A_0 e^{\mp i\phi_{\text{CEP}}} \int_{-\infty}^{\infty} d\tau f(\tau) e^{-i(\varepsilon_i \pm \omega)\tau + iS_V(\tau)}, \quad (6)$$

$$\mathcal{F}_2[f; \mathbf{p}] = \int_{-\infty}^{\infty} d\tau \mathbf{A}^2(\tau) e^{-i\varepsilon_i \tau + iS_V(\tau)}. \quad (7)$$

Using the rotational symmetry of the single-electron atomic Hamiltonian  $H_A$ , the initial bound state of the active electron can be characterized by its principal quantum number  $n$  as well as the orbital angular momentum  $\ell$  and its projection  $m$ , quite analogously to a hydrogenic atom. Together with its spin component  $\chi_{s, m_s}$ , this state has the well-known form

$$\begin{aligned} |\Psi_i(t)\rangle &= e^{-i\varepsilon_i t} |\psi_i\rangle = e^{-i\varepsilon_i t} |n \ell m\rangle \otimes |\chi_{s, m_s}\rangle \\ &\propto \frac{P_{n\ell}(r)}{r} Y_{\ell m}(\vartheta, \varphi) e^{-i\varepsilon_i t} \chi_{s, m_s}, \end{aligned} \quad (8)$$

where  $P_{n\ell}(r)/r$  denotes the radial wave function. The electron continuum in the laser field is given by Volkov-type states which, similarly, can be expanded into (distorted) partial

Hamiltonian  $H_A = \mathbf{p}^2/2 + V(\mathbf{r})$ , with the (effective) potential  $V(\mathbf{r})$  due to the nucleus and the other electrons. After its ionization, the electron is assumed to only move within the laser field and hence to just follow the Hamiltonian  $H_{1e} = [\mathbf{p} + \mathbf{A}(t)]^2/2$ . With these two assumptions in mind, the transition amplitude

$$T(\mathbf{p}) = T_0(\mathbf{p}) + T_1(\mathbf{p})$$

can be written in terms of the amplitudes  $T_0(\mathbf{p})$  and  $T_1(\mathbf{p})$ , which distinguish between the directly emitted and the rescattered photoelectrons, respectively. They are often briefly referred to as direct and rescattering amplitudes.

In our recent work [18] we demonstrated that the direct SFA amplitude can be expressed as

waves

$$\begin{aligned} |\chi_p(t)\rangle &= \sqrt{\frac{2}{\pi}} e^{-iS_V(t)} \sum_{\ell_p=0}^{\infty} \sum_{m_p=-\ell_p}^{\ell_p} Y_{\ell_p m_p}^*(\vartheta_p, \varphi_p) |\varepsilon_p \ell_p m_p\rangle \\ &\otimes |\chi_{s', m'_s}\rangle \end{aligned} \quad (9)$$

and characterized by their energy  $\varepsilon_p = p^2/2$  as well as the orbital angular momentum quantum numbers  $\ell_p$  and  $m_p$ , respectively. In the velocity gauge, the interaction between the continuum electron and laser field is thereby accounted for by the so-called Volkov phase

$$S_V(t) = \frac{1}{2} \int^t d\tau [\mathbf{p} + \mathbf{A}(\tau)]^2. \quad (10)$$

In the representation of the direct amplitude (5), the interaction of the photoelectron with the remaining photoion can be readily considered by means of the radial wave functions  $P_{\varepsilon_p \ell_p}(r)$  as defined by

$$\langle \mathbf{r} | \varepsilon_p \ell_p m_p \rangle = i^{\ell_p} \frac{P_{\varepsilon_p \ell_p}(r)}{r} Y_{\ell_p m_p}(\vartheta, \varphi).$$

Apart from a plane wave

$$P_{\varepsilon_p \ell_p}(r) = r j_{\ell_p}(pr), \quad (11)$$

as originally assumed in the SFA with the spherical Bessel functions  $j_{\ell}(x)$ , this radial function can be approximated by

either a Coulomb wave

$$P_{\varepsilon_p \ell_p}(r) = w_{\ell_p}(\eta_p, pr) = \frac{1}{p} e^{i\sigma_{\ell_p}} F_{\ell_p}(\eta_p, pr) \quad (12)$$

or any distorted wave as common in atomic structure theory. Moreover, in Eq. (12) the functions  $F_{\ell_p}(\eta_p, pr)$  are, as known, often expressed in terms of hypergeometric functions, where  $\sigma_{\ell_p}$  denotes the Coulomb phase shift [18].

The form (5) of the transition amplitude above enables one to implement a number of physical scenarios (approximations) for modeling the ATI in terms of different partial waves but without the need for further analytical work. In the next section we will make use of this expansion to proceed one step further and to express the amplitude in a basis of coupled angular momenta. Apart from the simplification of expression (5), it is *this* form of coupled wave functions and, potentially, configuration expansions that will enable one to combine the SFA with atomic structure theory and to readily explore the contributions due to the fine structure (coupling) or the correlated motion of many-electron systems in the future.

### B. Use of a coupled angular momentum basis

Instead of dealing separately with the orbitals  $(\ell, m)$  and spin angular momenta  $(s, m_s)$ , they are often coupled right

from the beginning to the total angular momentum  $(j, m_j)$ . We make use of this coupling for both the initial and final continuum states. Let us note, however, that the simple multiplication of the continuum waves by the (purely time-dependent) Volkov phase factor  $e^{-iS_V(t)}$  is a result of the dipole approximation and cannot be ensured so easily if the approximation is abandoned [21,23]. In the electric dipole approximation, different expansions of the *spatial* part of these states can be applied rather easily. If we replace the initial and continuum states from above by

$$|\Psi_i(t)\rangle = e^{-i\varepsilon_i t} |n\ell j m_j\rangle \quad (13)$$

and

$$\begin{aligned} |\chi_{\mathbf{p}, m'_s}(t)\rangle &= \sqrt{\frac{2}{\pi}} e^{-iS_V(t)} \sum_{\ell_p=0}^{\infty} \sum_{m_p=-\ell_p}^{\ell_p} \sum_{j_p \geq 1/2} Y_{\ell_p m_p}^*(\vartheta_p, \varphi_p) \\ &\times \langle \ell_p m_p, \frac{1}{2} m'_s | j_p, m_p + m'_s \rangle \langle \varepsilon_p \ell_p j_p, m_p + m'_s \rangle, \end{aligned} \quad (14)$$

we can follow Ref. [18] and rewrite the direct SFA transition amplitude (5) within the coupled basis as

$$\begin{aligned} T_0(\mathbf{p}, m_j, m'_s) &= -\frac{i}{\sqrt{2\pi}} \mathcal{F}_1[\omega; f; \mathbf{p}] \left( \sum_{\ell_p=0}^{\infty} \sum_{j_p \geq 1/2} \sum_{q=0, \pm 1} (-1)^q u_q Y_{\ell_p, m_j - m'_s - q}(\vartheta_p, \varphi_p) \right. \\ &\times \langle \ell_p(m_j - m'_s - q), \frac{1}{2} m'_s | j_p(m_j - q) \rangle \langle j m_j, 1(-q) | j_p(m_j - q) \rangle \langle \varepsilon_p \ell_p j_p \| \mathbf{p} \| n\ell j \rangle \left. \right) \\ &- \frac{i}{\sqrt{2\pi}} \mathcal{F}_1[-\omega; f; \mathbf{p}] \left( \sum_{\ell_p=0}^{\infty} \sum_{j_p \geq 1/2} \sum_{q=0, \pm 1} u_q^* Y_{\ell_p, m_j - m'_s + q}(\vartheta_p, \varphi_p) \right. \\ &\times \langle \ell_p(m_j - m'_s + q), \frac{1}{2} m'_s | j_p(m_j + q) \rangle \langle j m_j, 1q | j_p(m_j + q) \rangle \langle \varepsilon_p \ell_p j_p \| \mathbf{p} \| n\ell j \rangle \left. \right) \\ &- \frac{i}{\sqrt{2\pi}} \mathcal{F}_2[f; \mathbf{p}] Y_{\ell_p, m_j - m'_s}(\vartheta_p, \varphi_p) \langle \ell(m_j - m'_s), \frac{1}{2} m'_s | j m_j \rangle \langle \varepsilon_p \ell j m_j | n\ell j m_j \rangle. \end{aligned} \quad (15)$$

As before in Eq. (5), all properties of the driving laser pulse are entirely encoded into the pulse-shape integrals (6), which account for the Volkov phase as well. The spatial dependence of both the initial and continuum electron states remains again in the reduced matrix elements  $\langle \varepsilon_p \ell_p j_p \| \mathbf{p} \| n\ell j \rangle$  of the momentum operator. It is instructive to expand the initial and continuum states back into the uncoupled basis, i.e., to use

$$\begin{aligned} |n\ell j\rangle &= \sum_{m=-\ell}^{\ell} \sum_{m_s=\pm 1/2} | \ell m, \frac{1}{2} m_s \rangle \langle \ell m, \frac{1}{2} m_s | j m_j \rangle, \\ \langle \varepsilon_p \ell_p j_p \rangle &= \sum_{m_p=-\ell_p}^{\ell_p} \sum_{m'_s=\pm 1/2} | \ell_p m_p, \frac{1}{2} m'_s \rangle \langle \ell_p m_p, \frac{1}{2} m'_s | j_p m'_s \rangle. \end{aligned}$$

Based on these expressions, one can write the reduced matrix elements within the coupled basis in terms of the reduced matrix elements from the uncoupled basis,

$$\langle \varepsilon_p \ell_p j_p \| \mathbf{p} \| n\ell j \rangle = \left( \sum_{m=-\ell}^{\ell} \sum_{m_p=-\ell_p}^{\ell_p} \sum_{m_s=\pm 1/2} \langle \ell_p m_p, \frac{1}{2} m_s | j_p(m_p + m_s) \rangle \langle \ell m, \frac{1}{2} m_s | j(m + m_s) \rangle \right) \langle \varepsilon_p \ell_p \| \mathbf{p} \| n\ell \rangle.$$

If the radial wave functions are explicitly known, the reduced matrix elements can be evaluated via [18]

$$\langle \varepsilon_p \ell_p \mathbf{p} \| \mathbf{P} \| n \ell \rangle = (-i)^{\ell_p+1} \langle \ell_p \| \mathbf{C}^1 \| \ell \rangle \int_0^\infty dr \frac{P_{\varepsilon_p \ell_p}^*(r)}{r} \left( r \frac{\partial P_{n\ell}(r)}{\partial r} - \frac{(\ell_p - \ell)(\ell_p + \ell + 1)}{2} P_{n\ell}(r) \right). \quad (16)$$

Since the matrix elements in Eq. (15) often occur in atomic computations, they can be readily obtained from different codes known in the literature [24]. At the first glance, the expression (15) for the transition amplitude appears to be more complicated than the amplitude (5) due to the coupling of the spin and orbital angular momenta. In strong-field processes, the spin quantum number of the outgoing electron can usually be treated independently and then leads to a Kronecker delta [25]. In many-electron targets, however, this only applies if the spin-orbit interaction is negligible and if the antisymmetry of the wave functions is handled manually. To readily include this (well-known) interaction and to combine the SFA formalism with atomic theory, a coupled basis is mandatory and will help expand the formalism towards few- and many-electron systems.

### C. Implementation

The direct SFA transition amplitude (15) in the coupled angular momentum basis facilitates the computation of photoelectron energy spectra and momentum or angular distributions. However, in order to obtain experimentally meaningful results for the photoionization probability (4), we still need to average and sum over all spin and angular momentum projections of the initial and final states,

$$\mathbb{P}(\mathbf{p}) = \frac{1}{2} \frac{P}{2\ell + 1} \sum_{m=-\ell}^{\ell} \sum_{m_s=\pm 1/2} \sum_{m'_s=\pm 1/2} |T(\mathbf{p}, m, m_s, m'_s)|^2 \quad (17)$$

$$= \frac{P}{2j + 1} \sum_{m_j=-j}^j \sum_{m'_s=\pm 1/2} |T(\mathbf{p}, m_j, m'_s)|^2, \quad (18)$$

where  $T(\mathbf{p}, m, m_s, m'_s)$  and  $T(\mathbf{p}, m_j, m'_s)$  are given by Eqs. (5) and (15), respectively. Since both expressions are related to each other by just a change of the (single-electron) basis, the (numerical) results are of course identical. In practice, however, the coupling of angular momenta not only simplifies the computations, but enables one to incorporate relativistic terms or to exploit them in many-electron atomic structure computations. Similar to the standard SFA, the reduced matrix elements in the amplitude (15) can still be obtained by applying analytical expressions for hydrogenic initial states and plane-wave Volkov states [10,26]. To analyze the Coulomb asymmetry in the angular distributions below, all the different approximations for evaluating the reduced matrix elements  $\langle \varepsilon_p \ell_p \mathbf{p} \| \mathbf{P} \| n \ell \rangle$  or  $\langle \varepsilon_p \ell_p j_p \mathbf{p} \| \mathbf{P} \| n \ell j \rangle$  have been implemented within the JENA ATOMIC CALCULATOR [27]. In this toolbox, the initial bound and final continuum orbitals are obtained as part of a self-consistent-field procedure. In these computations, a Hartree-Fock-Slater potential has been applied in order to account for the repulsion and exchange interaction among all bound electrons and to obtain binding

energies within about 5–10%, when compared to experiment. In contrast, the continuum orbitals of the targets below are generated as usual in the *static* potential of the singly charged photoion and for the energies as measured at the detector [28].

Below we make use of the various approximations for the initial bound and final continuum states in order to disentangle the role of different contributions to the ATI energy spectra and the (Coulomb asymmetry in the) angular distribution for different target atoms.

### III. NUMERICAL RESULTS

Four different approximations are selected below to understand how the ATI energy spectra and angular distributions depend on the choice of the initial and final continuum states; they are all based on the SFA amplitude (15) and the associated ionization probability  $\mathbb{P}(\mathbf{p})$ . In this amplitude, different radial orbital functions enter in particular the reduced matrix elements and then lead to different predictions. To cover a good range of light and medium elements, calculations are performed for the atomic targets lithium, argon, and xenon and are compared with measured spectra from the literature for argon and xenon.

(i) *Hydrogenic approximation.* A hydrogenlike  $1s$  initial state has an effective nuclear charge and plane-wave Volkov continuum states (11); the nuclear charge for this hydrogenic state has been chosen to reproduce the ionization potential of the target atoms (lithium, 5.39 eV; argon, 15.76 eV; and xenon, 12.13 eV).

(ii) *Hydrogenic Coulomb approximation.* A hydrogenlike  $n\ell$  initial state has an effective nuclear charge as above and an active electron from the valence shell of the target atoms (lithium,  $2s$ ; argon,  $3p$ ; and xenon,  $5p$ ) as well as the final Coulomb-Volkov continuum states (12).

(iii) *Atomic Coulomb approximation.* We use an atomic initial state (cf. Sec. IIC) and final Coulomb-Volkov continuum states to evaluate the reduced matrix elements in Eq. (15).

(iv) *Atomic approximation.* Atomic initial and distorted Volkov continuum states are used to calculate all reduced matrix elements (cf. Sec. IIC).

In all these model computations, we moreover assume some  $n_p = 8$  cycle elliptically polarized laser pulses with ellipticity  $\epsilon$ , wavelength 800 nm ( $\omega = 0.057$  a.u.), and carrier-envelope phase  $\phi_{\text{CEP}} = 0$ . In order to compare these computations with experiment, we have chosen  $\epsilon = 0.25$  (lithium and argon),  $\epsilon = 0.36$  (xenon), and  $\epsilon = 0.56$  (lithium, argon, and xenon) as well as the two intensities  $I = 0.9 \times 10^{14}$  and  $1.5 \times 10^{14}$  W/cm<sup>2</sup> and compare these results for  $\epsilon = 0.25$  (argon) as well as  $\epsilon = 0.36$  and  $0.56$  (xenon) with experimental data available in the literature. All these parameters together specify the vector potential (2) and hence the laser-electron interaction operator completely.

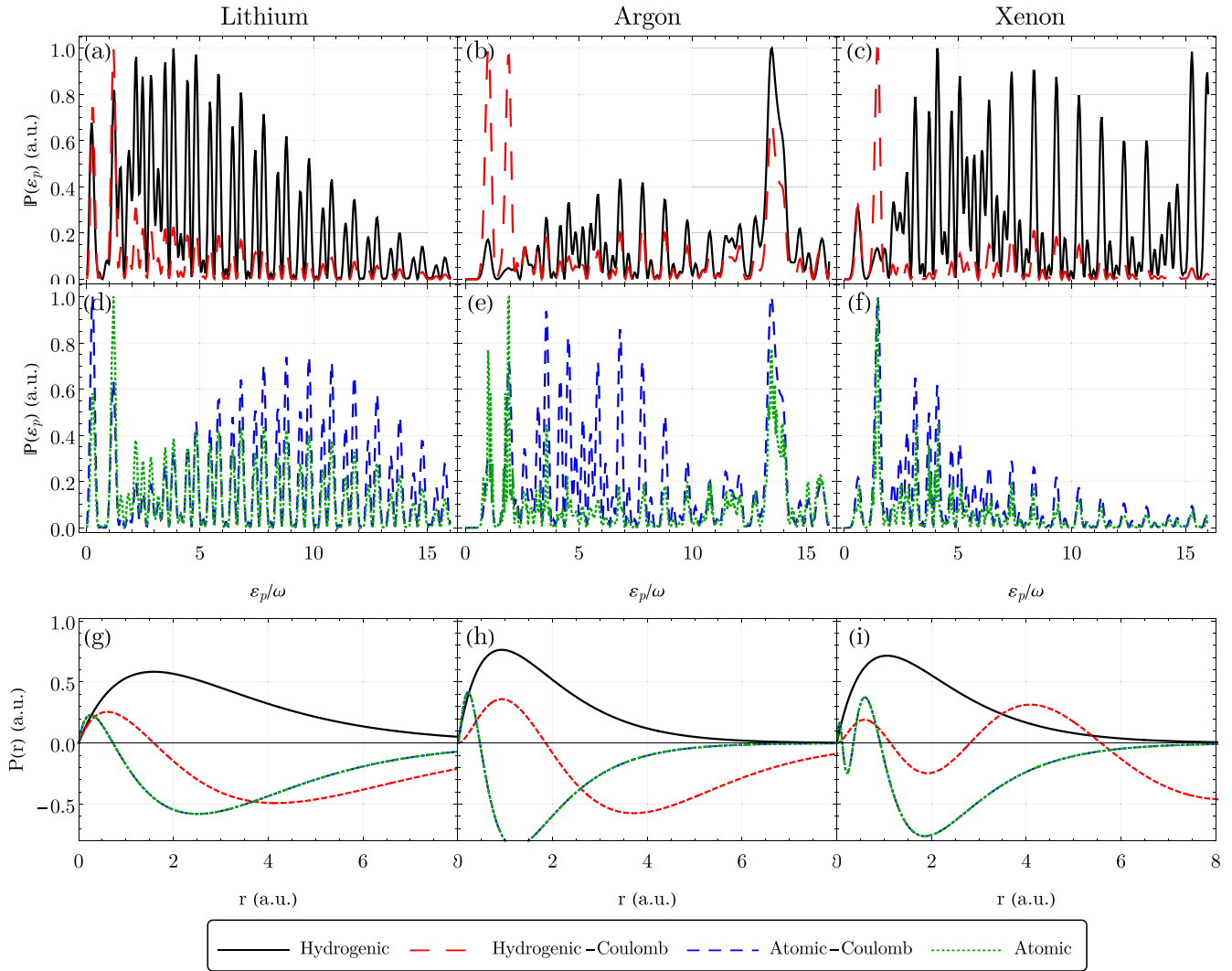


FIG. 2. ATI energy spectra of photoelectrons emitted along the major axis of the polarization ellipse ( $x$  axis) for (a), (d), and (g) lithium, (b), (e), and (h) argon, and (c), (f), and (i) xenon and for an  $n_p = 8$  cycle laser pulse with ellipticity  $\epsilon = 0.36$ . The spectra in (a)–(c) were computed in the hydrogenic (black solid curves) and the hydrogenic Coulomb approximations (red long-dashed curves); in (d)–(f) use was made of the atomic Coulomb (blue short-dashed curves) and atomic approximation (green dotted curves). All these spectra are normalized on their maximum. (g)–(i) Radial wave functions  $P(r)$  of the associated initial states: hydrogenic (black solid curves), hydrogenic Coulomb (red dashed curves), and atomic (green dash-dotted curves). A laser pulse with wavelength  $\lambda = 800$  nm and intensity  $I = 0.9 \times 10^{14}$  W/cm<sup>2</sup> was used in all these computations.

### A. Photoelectron energy spectra

Let us begin with calculating the photoelectron energy spectra (ATI spectra) for the given targets and by using the four approximations from above. Figures 2 and 3 display the calculated spectra for  $\epsilon = 0.36$  and  $0.56$ , respectively. In Figs. 2(g)–2(i), moreover, the radial wave functions of the initial states are shown for these approaches.

Many ATI experiments have been performed with either noble-gas or alkali-metal targets. For these targets, the measured ATI spectra are often well reproduced, at least qualitatively, within the hydrogenic SFA above, i.e., by applying a hydrogenic  $1s$  initial state in the computation of the direct amplitude (15). In particular, the positions of individual ATI peaks in the energy spectra are known to be determined almost entirely by the Volkov phase (10) and as readily seen from Figs. 3(a)–3(f). In all four approximations, indeed, the energy

spectra peak at almost identical positions, quite independently of how the initial and final wave functions were chosen.

Apart from the ionization potential, however, the SFA amplitude (15) depends via the reduced matrix element  $\langle \epsilon_p \ell_p j_p \| \mathbf{p} \| n \ell j \rangle$  also on the detailed form of the initial bound and final continuum states. The role of the initial states upon the photoelectron energy spectra has been discussed previously in Refs. [29,30] by comparing, for instance, the spectra for hydrogenic  $1s$  and  $n\ell$  initial states of the target atoms. We therefore expect that a realistic description of the atomic target helps improve the predicted spectra and their agreement with experiment. With the formulation of the direct amplitude (15) above, we therefore provide a modular way to replace the initial bound and final continuum states [18,31]. This procedure is quite in contrast and much simpler than most previous studies, in which elaborate analytical reformulations

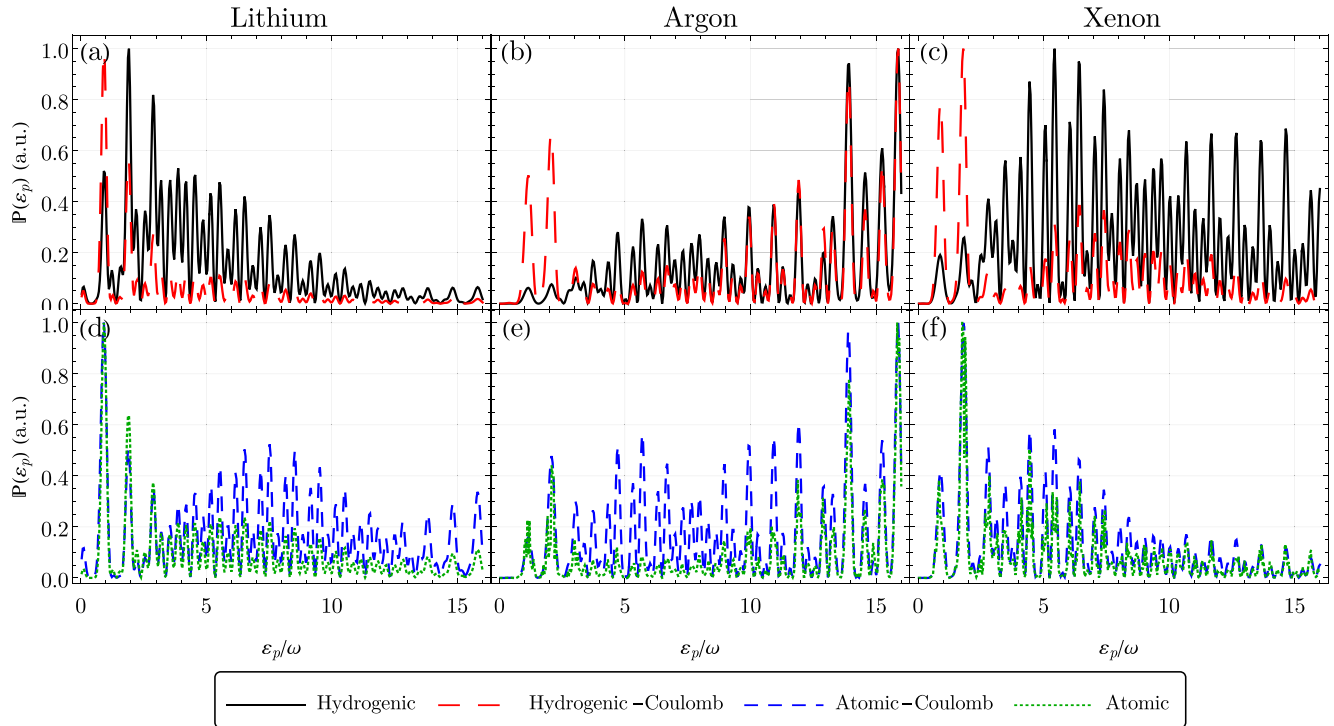


FIG. 3. Same as in Figs. 2(a)–2(f) but for the ellipticity  $\epsilon = 0.56$  of the driving beam.

were performed in order to incorporate approximate atomic states into the SFA [32].

As seen from Figs. 2 and 3, the original hydrogenic approximation (black solid curves) strongly differ from all the other spectra. This difference might be expected, perhaps, as the wave function of the active target electron has little in common with the  $1s$  (radial) function, and this still remains true if the nuclear charge is scaled to the ionization potential. This is seen also from Figs. 2(g)–2(i). While the positions of the ATI peaks in the spectra are affected mainly via the Volkov phase by the temporal structure of the laser pulse, their (absolute) values are rather different because of the detailed shape of the wave functions or, speaking more technically, the reduced matrix elements of the momentum operator in the direct amplitude (15).

Besides the initial bound state, the continuum states exhibit an even greater effect upon the energy spectra. A plane-wave Volkov continuum only works well for rather high photoelectron energies. This is seen particularly for xenon in Figs. 2(c) and 2(f) and similarly in Figs. 3(c) and 3(f). Apart from the hydrogenic approximation (black solid curves), the magnitudes of individual peaks are almost identical for all other approximations and for sufficiently high photoelectron energies  $\epsilon_p$ . In the low-energy region, in contrast, the ionization probabilities with plane-wave Volkov states are known to strongly deviate from experiment [33]. For low energies, the predictions have been improved by including the Coulomb potential of the residual ion in the continuum [34,35]. In the computational framework above [27,36], this is easily done by replacing the plane-wave Volkov states (11) by the Coulomb-Volkov states (12). The impact of the Coulomb-Volkov continuum can be seen particularly in the ATI energy spectra of argon and xenon in Fig. 2. In these spectra, both the hydrogenic Coulomb

(red long-dashed curves) and atomic Coulomb approximations (blue short-dashed curves) display considerably larger ionization probabilities when compared with the hydrogenic solutions (black solid curves) at low energies.

The differences between the hydrogenic and hydrogenic Coulomb approximations exemplifies first of all how the low-energy photoelectrons are affected by the Coulomb potential of the parent ion. They also demonstrate that the SFA is suitable for quite different strong-field regimes, provided the correct building blocks are applied in the formalism [31]. Still, the hydrogenic Coulomb approximation simply models the atomic potential by its (asymptotic) Coulomb behavior. As shown by Milošević and Becker [37], the low-energy part of the ATI spectra of noble gases can be improved further if a short-range potential is added to the Coulomb potential together with so-called atom Volkov states. This approach roughly corresponds to our atomic Coulomb approximation above. We can still proceed one step further by using distorted Volkov continuum states that are adapted to the particular target ions after the ionization has taken place. Figures 2 and 3(d)–3(f) compare the ATI energy spectra that are based on either a Coulomb-Volkov continuum (blue dashed curves) or a distorted Volkov continuum (green dotted curves). Since the initial state of the active electron is chosen to be the same in these spectra, the difference between the Coulomb-Volkov and distorted-Volkov curves entirely arises from this change of the continuum states in the SFA. While these two approximations still differ from each other, they particularly agree well in the low-energy part of the spectra. For these spectra, slightly larger differences remain for the two noble gases argon and xenon, for which the distorted Volkov approximation reduces the photoionization probabilities at low and medium photoelectron energies. Although perfect agreement

with experiment cannot be expected, the comparison of the ATI energy spectra in Figs. 2 and 3 may provide guidance to the theoretical modeling in those cases, in which the standard SFA formulation fails to explain the observations.

### B. Coulomb asymmetry in angular distributions

For elliptically polarized laser pulses, the (Coulomb) asymmetry in the photoelectron angular distribution was first observed by Bashkansky *et al.* [11] in the ATI of helium, krypton, and xenon gas targets. In their measurements, they recorded the azimuthal photoelectron angular distributions in the polarization plane at fixed energies and found that the distributions merely possess an inversion symmetry about the origin. This is in contrast to the (original) SFA based on a plane-wave Volkov continuum, which predicted mirror-symmetric angular distributions with regard to both the minor and major axes of the polarization ellipse [12]. While this mirror symmetry can be readily understood by the plane-wave Volkov continuum, it is seen experimentally only in the strong-field ionization of negatively charged anions [38].

Inspired by these observations, several theoretical studies were carried out and showed that the predicted mirror symmetry in the SFA just arises from neglecting the ionic potential for the outgoing photoelectrons [39–41]. In a subsequent semiclassical simulation by Goreslavski *et al.* [12], the correct symmetry of the angular distribution was obtained by just including the Coulomb field in the classical equations of motion. Moreover, in this work the observed angular distributions for xenon targets were shown for different ellipticities, which, since then, have often been used as a benchmark for theoretical calculations. Indeed, several studies have meanwhile been performed in order to explore how the pulse duration and further laser parameters as well as the target potential affect the shape and orientation of the photoelectron angular distributions [14, 17, 42, 43]. Despite all these efforts, however, most of the calculated angular distributions have not agreed well with experiment and mainly recover the more or less correct asymmetry within the polarization plane.

Therefore, the Coulomb asymmetry in the angular distribution of strong-field ionized atomic targets provide an excellent test bed for analyzing and comparing the (four) approximations above. Figure 4 displays such angular distributions for the ATI with elliptically polarized laser beams for lithium, argon, and xenon targets. All these angular distributions are taken within the polarization plane ( $\vartheta_p = \pi/2$ ) but for beams with different ellipticity and intensity. For the sake of comparison, they are shown for the ATI peaks that refer to fixed photoelectron energies  $\epsilon_p$  between  $4\omega$  and  $5\omega$  above the threshold. The purple dash-dotted curves in this figure display the experimental distributions for argon [14] ( $\epsilon = 0.25$ ) and xenon [12] ( $\epsilon = 0.36$  and  $0.56$ ). All these experimental curves clearly possess inversion symmetry but do not exhibit any mirror symmetry with regard to the horizontal or vertical axes.

We can compare these observations with the different approximations above as obtained for the direct SFA amplitude (5). The black solid curves in Fig. 4, for example, show the angular distributions from the hydrogenic approximation. Owing to the symmetry of the vector potential of the driving beam, that is, the symmetry of the polarization ellipse,

these distributions must be mirror symmetric with respect to the major ( $x$ ) and minor ( $y$ ) axes. This symmetry of the angular distribution is however *distorted* (and rotated; cf. the red dashed curves in Fig. 4), if the plane-wave Volkov states are replaced by Coulomb-Volkov states. Therefore, the hydrogenic Coulomb approximation already predicts a Coulomb asymmetry of the angular distributions, although their distributions are still quite different when compared to measurements for argon and xenon. If we also replace the (hydrogenic) initial state of the active electron by a more realistic wave function in the atomic Coulomb approximation, the deviations from experiment increase again. Indeed, the blue dashed distributions exhibit a clearly reduced asymmetry when compared to the red dashed distributions, as they are rotated back towards the horizontal axis in all the panels of Fig. 4.

In the atomic approximation (green dotted curves in Fig. 4), we finally include also the ionic potential for the outgoing photoelectrons. In this approximation, the maxima of the lobes are found to be in quite reasonable agreement with the observed distributions. For the two ellipticities  $\epsilon = 0.25$  (argon) and  $\epsilon = 0.36$  (xenon), however, the experimental distributions are already (fully) inversion symmetric, while our best approximation still exhibit two lobes with quite different maxima. One reason for this behavior is the limited duration of the driving laser pulse as applied in the computations. Figure 5 compares the angular distribution for laser pulses of different durations for a xenon target and  $\epsilon = 0.56$ . The green dotted curve is identical to the green dotted curve in Fig. 4(f). As easily seen from Fig. 5, the two lobes of the angular distributions becomes (nearly) the same as the pulse duration, i.e., the number of optical cycles, increases. An analogous behavior is expected for the remaining asymmetries in the curves of Fig. 4. At present, however, our numerical implementation does not enable us to deal with pulses longer than  $n_p \approx 8$  optical cycles because of numerical instabilities due to the highly oscillating pulse shape integrals.

Particularly for xenon and  $\epsilon = 0.56$ , the lobes are wider than the experimental ones. Further work will be needed to understand these differences which might result from the velocity gauge for the coupling of the radiation field or from omitted contributions in the amplitude (5). While all other theoretical distributions in Figs. 4(a), 4(c), and 4(e) show a rather similar structure, the full inversion symmetry with regard to the maxima in the angular distributions may indeed require one to use the length gauge. Unfortunately, however, this length gauge is technically more complicated since the time and radial integration can no longer be separated in a simple manner. An implementation of this length gauge is therefore beyond the scope of the present work. In addition, the rescattering of photoelectrons at their parent ions may have a measurable influence for  $\epsilon = 0.25$  and should be examined further. In most of our approximations above, we also found a visible rotation of the angular distribution if the intensity of the laser pulse is changed by just a few percent. For lithium and  $\epsilon = 0.56$ , for example, a change of intensity from  $I = 0.9 \times 10^{14}$  to  $0.93 \times 10^{14}$  W/cm<sup>2</sup> leads to almost identical distributions of our computations with experiment. Therefore, parts of the remaining disagreement between experimental and theoretical distributions in Fig. 4

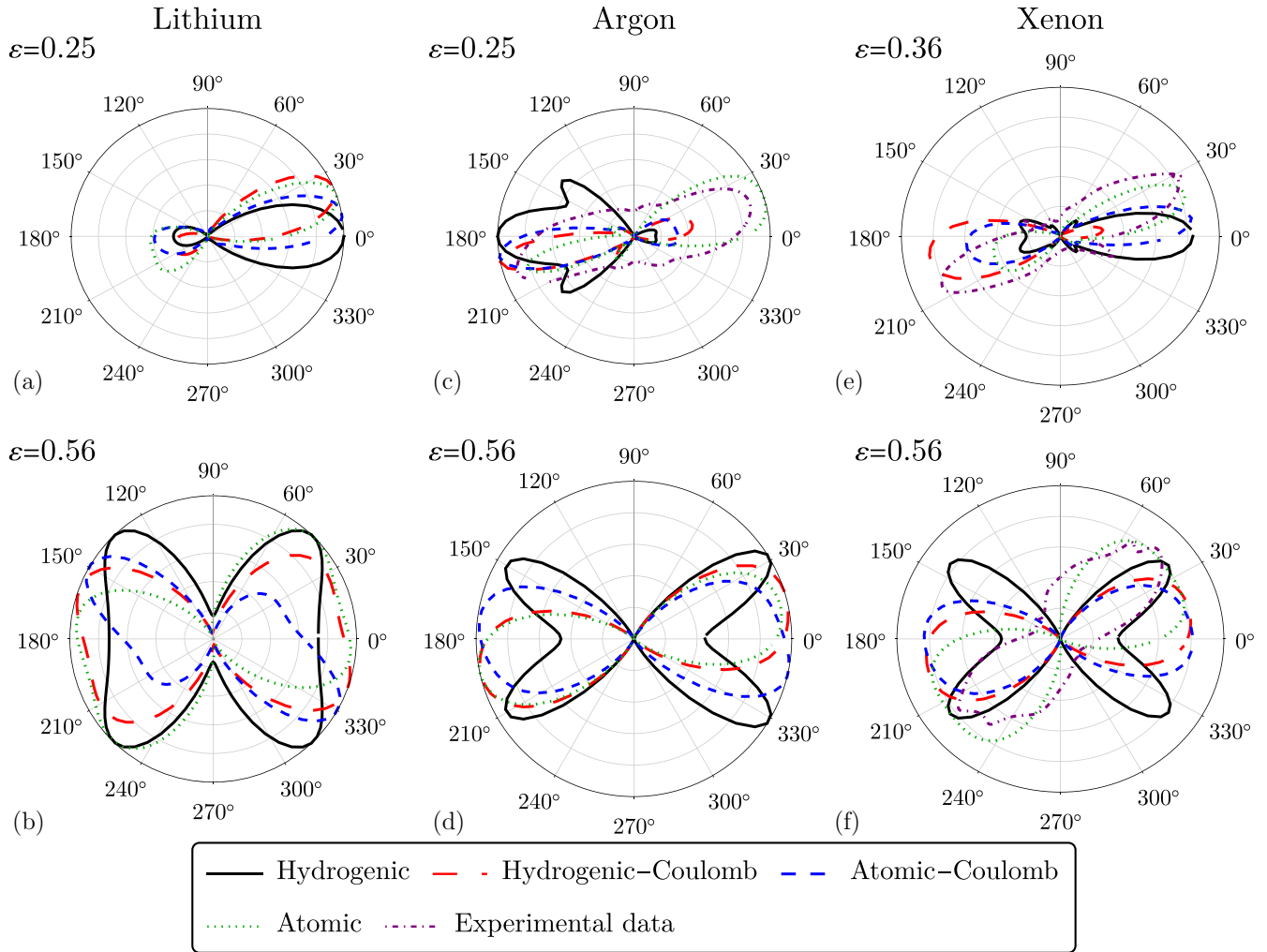


FIG. 4. Comparison of photoelectron angular distributions from the ATI with elliptically polarized  $n_p = 8$  cycle laser beams for three different target atoms: (a) and (b) lithium, (c) and (d) argon, and (e) and (f) xenon. All these angular distributions are taken within the polarization plane ( $\vartheta_p = \pi/2$ ) and for beams with ellipticities  $\epsilon = 0.25$  and  $0.56$  and intensity  $I = 1.5 \times 10^{14}$  W/cm<sup>2</sup> for lithium and argon as well as with  $\epsilon = 0.36$  and  $0.56$  and intensity  $I = 0.9 \times 10^{14}$  W/cm<sup>2</sup> for xenon, respectively. They are shown for the ATI peaks that refer to fixed photoelectron energies  $\epsilon_p$  between  $4\omega$  and  $5\omega$  above the threshold. These energies also slightly vary for the different approximations and targets for which the wave functions were generated (cf. Figs. 2 and 3). For the sake of comparison, again, all these distributions are normalized on their maximum. Angular distributions from different approximations are compared in each of these polar plots: hydrogenic (black solid curves), hydrogenic Coulomb (red long-dashed curves), atomic Coulomb (blue short-dashed curves), and atomic (green dotted curves). In addition, measured distributions from Refs. [14] (argon) and [12] (xenon) are displayed as well (purple dash-dotted curves). All other laser parameters are the same as in Fig. 2.

may arise from the uncertainties of the experimental intensity.

For the ellipticity  $\epsilon = 0.56$ , the correct inversion symmetry is found for all predicted angular distributions as seen from Figs. 4(b), 4(d), and 4(f). Particularly for xenon, the angular distribution from the atomic approximation (green dotted curves) are in good agreement with experiment and significantly better than for any of the other approximations. The use of a target-specific distorted Volkov continuum for the outgoing electron helps improve the angular distributions and forms a clear contrast to the typically applied Coulomb-Volkov states in recent SFA computations. Similar good agreement with available observations has been found also for other photoelectron energies.

Despite all these improvements due to the use of the target-adapted initial bound and final continuum states, some discrepancies remain between experiment and our predictions above. Possible reasons for these discrepancies may refer to the (incomplete) knowledge of the intensity and time structure of the laser pulses, as indicated above.

#### IV. CONCLUSION

A partial-wave representation of the SFA has been developed and applied to calculate the ATI photoelectron spectra and angular distributions for different atomic targets. This representation enables one to combine the (basic assumptions of the) SFA with concepts from atomic structure theory [27,31].

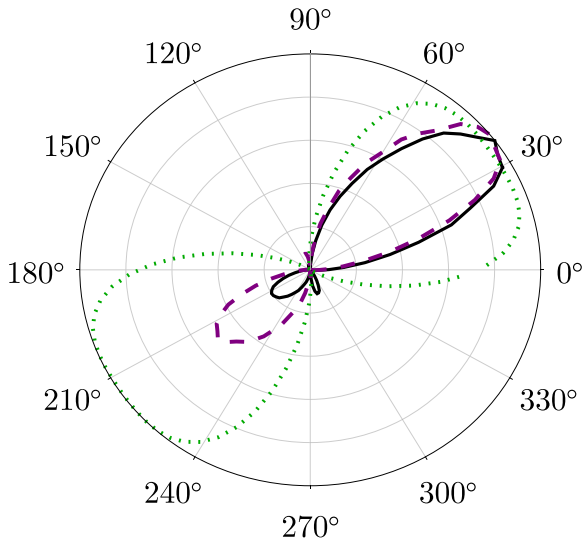


FIG. 5. Photoelectron angular distributions in the atomic approximation for three different pulse lengths or number of optical cycles:  $n_p = 2$  (black solid curve),  $n_p = 4$  (purple dashed curve), and  $n_p = 8$  (green dotted curve). All curves were computed in the atomic approximation and for a xenon target, the wavelength  $\lambda = 800$  nm, laser intensity  $I = 0.9 \times 10^{14}$  W/cm<sup>2</sup>, and an ellipticity  $\epsilon = 0.56$ . All curves are normalized on their maxima.

Following our previous work [18], the target-specific initial bound and final continuum states have been applied in a basis of coupled angular momenta in order to include the spatial and spin motion of the active electron(s) on equal footing.

In this work we particularly show and discuss how different approximations to the SFA can be readily utilized to stepwise improve the initial and continuum states (wave functions). Apart from using hydrogenic initial and plane-wave Volkov continuum states, i.e., by following the original formulation of the SFA, a target-specific initial bound and a distorted-wave continuum help improve the calculated spectra or angular distributions. These improvements put the predicted spectra in reasonable agreement with experiment. We therefore conclude that a proper treatment of the target wave functions is essential for predicting the ATI energy spectra also *quantitatively*.

In addition, we have studied the Coulomb asymmetry in the photoelectron angular distributions following the ionization by elliptically polarized laser pulses. While this asymmetry is known to arise from the (Coulombic) interaction of the photoelectron with its parent ion, the use of target-adapted initial bound and distorted-Volkov continuum states generally gives rise to the best agreement with experiment. Detailed computations have been performed for lithium, argon, and xenon targets. Although some deviations from experiment remain for argon and xenon, further studies for small ellipticities of the driving beam are desirable within the length gauge and by including also the rescattering amplitude in the computation of the ionization probabilities.

Still, several further extensions to the SFA remain preferable. For the ATI process, a coupling to other atomic bound states could be incorporated as well within the partial-wave representation. This representation will enable us also to account for nondipole contributions from the interaction with the radiation field by just including reduced matrix elements beyond the electric dipole terms [21,23]. Furthermore, a simpler expansion of the SFA amplitude might be performed for other strong-field processes, such as high-order harmonic generation and nonsequential double ionization [19,44]. Since all these “second-order” processes (with regard to the number of interactions of the atomic electrons) arise from either a recombination or rescattering between the photoelectron and photoion, we expect that a realistic description of the target atom will have a significant impact upon all predictions. Finally, one can formally rewrite the SFA amplitude (15) also in terms of (correlated) many-electron states by using partial waves and spherical tensor operators as described above, where the single-electron matrix elements from above then need to be replaced by corresponding many-electron amplitudes as they frequently occur in atomic structure theory.

#### ACKNOWLEDGMENT

This work was funded by the Deutsche Forschungsgemeinschaft (German Research Foundation) under Project No. 440556973.

- [1] L. Gallmann, C. Cirelli, and U. Keller, *Annu. Rev. Phys. Chem.* **63**, 447 (2012).
- [2] P. Agostini, F. Fabre, G. Mainfray, G. Petite, and N. K. Rahman, *Phys. Rev. Lett.* **42**, 1127 (1979).
- [3] G. G. Paulus, W. Nicklich, H. Xu, P. Lambropoulos, and H. Walther, *Phys. Rev. Lett.* **72**, 2851 (1994).
- [4] B. Walker, B. Sheehy, L. F. DiMauro, P. Agostini, K. J. Schafer, and K. C. Kulander, *Phys. Rev. Lett.* **73**, 1227 (1994).
- [5] A. McPherson, G. Gibson, H. Jara, U. Johann, T. S. Luk, I. A. McIntyre, K. Boyer, and C. K. Rhodes, *J. Opt. Soc. Am. B* **4**, 595 (1987).
- [6] M. Ferray, A. L’Huillier, X. F. Li, L. A. Lompre, G. Mainfray, and C. Manus, *J. Phys. B* **21**, L31 (1988).
- [7] L. V. Keldysh, *Soviet Phys. JETP-USSR* **20**, 1307 (1965).
- [8] F. H. M. Faisal, *J. Phys. B* **6**, L89 (1973).
- [9] H. R. Reiss, *Phys. Rev. A* **22**, 1786 (1980).
- [10] D. B. Milošević, G. G. Paulus, D. Bauer, and W. Becker, *J. Phys. B* **39**, R203 (2006).
- [11] M. Bashkansky, P. H. Bucksbaum, and D. W. Schumacher, *Phys. Rev. Lett.* **60**, 2458 (1988).
- [12] S. P. Goreslavski, G. G. Paulus, S. V. Popruzhenko, and N. I. Shvetsov-Shilovski, *Phys. Rev. Lett.* **93**, 233002 (2004).
- [13] H. Xie, M. Li, S. Luo, Y. Li, Y. Zhou, W. Cao, and P. Lu, *Phys. Rev. A* **96**, 063421 (2017).
- [14] M. Li, Y. Liu, H. Liu, Q. Ning, L. Fu, J. Liu, Y. Deng, C. Wu, L.-Y. Peng, and Q. Gong, *Phys. Rev. Lett.* **111**, 023006 (2013).
- [15] F. H. M. Faisal and S. Förster, *J. Phys. B* **51**, 234001 (2018).

- [16] K. Amini, J. Biegert, F. Calegari, A. Chacón, M. F. Ciappina, A. Dauphin, D. K. Efimov, C. F. de Morisson Faria, K. Giergiel, P. Gniewek, A. S. Landsman, M. Lesiuk, M. Mandrysz, A. S. Maxwell, R. Moszyński, L. Ortmann, J. A. Pérez-Hernández, A. Picón, E. Pisanty, J. Prazdner-Bechcicki *et al.*, *Rep. Prog. Phys.* **82**, 116001 (2019).
- [17] Y. L. Wang, S. G. Yu, X. Y. Lai, X. J. Liu, and J. Chen, *Phys. Rev. A* **95**, 063406 (2017).
- [18] B. Böning and S. Fritzsche, *Phys. Rev. A* **102**, 053108 (2020).
- [19] F. Liu, Z. Chen, T. Morishita, K. Bartschat, B. Böning, and S. Fritzsche, *Phys. Rev. A* **104**, 013105 (2021).
- [20] A. C. Bray, A. S. Maxwell, Y. Kissin, M. Ruberti, M. F. Ciappina, V. Averbukh, and C. Figueira De Morisson Faria, *J. Phys. B* **54**, 194002 (2021).
- [21] B. Böning, W. Paufler, and S. Fritzsche, *Phys. Rev. A* **99**, 053404 (2019).
- [22] S. Fritzsche and B. Böning, *Phys. Rev. Res.* **4**, 033031 (2022).
- [23] B. Böning and S. Fritzsche, *J. Phys. B* **54**, 144002 (2021).
- [24] R. D. Cowan, *The Theory of Atomic Structure and Spectra* (University of California Press, Berkeley, 1981).
- [25] D. Zille, D. Seipt, M. Möller, S. Fritzsche, S. Gräfe, C. Müller, and G. G. Paulus, *J. Phys. B* **50**, 065001 (2017).
- [26] B. H. Bransden and C. J. Joachain, *Physics of Atoms and Molecules* (Prentice Hall, Harlow, 2003).
- [27] S. Fritzsche, *Comput. Phys. Commun.* **240**, 1 (2019).
- [28] S. Fritzsche, B. Fricke, and W.-D. Sepp, *Phys. Rev. A* **45**, 1465 (1992).
- [29] J. H. Bauer, *J. Phys. B* **41**, 185003 (2008).
- [30] J. H. Bauer, *J. Phys. B* **46**, 045601 (2013).
- [31] S. Fritzsche and B. Böning, *Atoms* **10**, 70 (2022).
- [32] B. Böning, P. Abele, W. Paufler, and S. Fritzsche, *J. Phys. B* **54**, 025602 (2021).
- [33] C. I. Blaga, F. Catoire, P. Colosimo, G. G. Paulus, H. G. Muller, P. Agostini, and L. F. DiMauro, *Nat. Phys.* **5**, 335 (2009).
- [34] W. Quan, Z. Lin, M. Wu, H. Kang, H. Liu, X. Liu, J. Chen, J. Liu, X. T. He, S. G. Chen, H. Xiong, L. Guo, H. Xu, Y. Fu, Y. Cheng, and Z. Z. Xu, *Phys. Rev. Lett.* **103**, 093001 (2009).
- [35] C. Y. Wu, Y. D. Yang, Y. Q. Liu, Q. H. Gong, M. Y. Wu, X. Liu, X. L. Hao, W. D. Li, X. T. He, and J. Chen, *Phys. Rev. Lett.* **109**, 043001 (2012).
- [36] S. Fritzsche, P. Palmeri, and S. Schippers, *Symmetry* **13**, 520 (2021).
- [37] D. B. Milošević and W. Becker, *Phys. Rev. A* **99**, 043411 (2019).
- [38] F. Dulieu, C. Blondel, and C. Delsart, *J. Phys. B* **28**, 3861 (1995).
- [39] P. Krstić and M. H. Mittleman, *Phys. Rev. A* **44**, 5938 (1991).
- [40] S. Basile, F. Trombetta, G. Ferrante, R. Burlon, and C. Leone, *Phys. Rev. A* **37**, 1050 (1988).
- [41] A. Jaroń, J. Kamiński, and F. Ehlötzky, *Opt. Commun.* **163**, 115 (1999).
- [42] J. Wu, M. Meckel, S. Voss, H. Sann, M. Kunitski, L. P. H. Schmidt, A. Czasch, H. Kim, T. Jahnke, and R. Dörner, *Phys. Rev. Lett.* **108**, 043002 (2012).
- [43] R. P. Sun, X. Y. Lai, W. Quan, S. G. Yu, Y. L. Wang, S. P. Xu, Z. L. Xiao, Y. Zhou, M. Z. Wei, M. Zhao, and X. J. Liu, *Phys. Rev. A* **98**, 053418 (2018).
- [44] W. Paufler, B. Böning, and S. Fritzsche, *Phys. Rev. A* **98**, 011401(R) (2018).